

Polarimetric data-based model for tissue recognition: supplement

CARLA RODRÍGUEZ,^{1,5}  ALBERT VAN EECKHOUT,¹  LAIA FERRER,¹ ENRIQUE GARCIA-CAUREL,²  EMILIO GONZÁLEZ-ARNAY,^{3,4} JUAN CAMPOS,¹ AND ANGEL LIZANA^{1,6} 

¹Grup d'Òptica, Physics Department, Universitat Autònoma de Barcelona, Bellaterra 08193, Spain

²LPICM, CNRS, Ecole Polytechnique, Institut Polytechnique de Paris, Palaiseau 91120, France

³Departamento de Anatomía, Histología y Neurociencia, Universidad Autónoma de Madrid, Madrid 28049, Spain

⁴Servicio de Anatomía Patológica, Hospital Universitario de Canarias, Santa Cruz de Tenerife 38320, Spain

⁵carla.rodriguez@uab.cat

⁶angel.lizana@uab.cat

This supplement published with The Optical Society on 15 July 2021 by The Authors under the terms of the [Creative Commons Attribution 4.0 License](https://creativecommons.org/licenses/by/4.0/) in the format provided by the authors and unedited. Further distribution of this work must maintain attribution to the author(s) and the published article's title, journal citation, and DOI.

Supplement DOI: <https://doi.org/10.6084/m9.figshare.14879835>

Parent Article DOI: <https://doi.org/10.1364/BOE.426387>

Polarimetric data-based model for tissue recognition: supplemental document

1. Complete image Mueller polarimeter description

The current study is performed by measuring the experimental Mueller matrices from different chicken samples at three different illumination wavelengths covering the visible range: 625 nm, 530 nm and 470 nm. To do so, a complete image Mueller polarimeter [1-4] is used (Fig. S1) Particularly, it is based on Parallel Aligned Liquid Crystals (PA-LC) retarders and consists of two compact and mobile arms. The first one, the Polarization State Generator (PSG), allows us to generate any fully polarized state so we can illuminate the sample with controlled polarized light. It is composed by a linear polarizer oriented at 0° followed by two PA-LC at 45° and 0° , respectively, with respect to the laboratory vertical. We illuminate the sample at 56° with respect to the vertical so the second arm, called Polarization State Analyzer (PSA) and placed in the vertical position avoids direct reflections and collects the scattered light. PSA is composed of the same elements as PSG but placed in the inverse order to finally capture, by means of a CCD camera, the sample's intensity image. With this architecture, the polarimeter is capable to analyze and determine the polarimetric response of the sample.

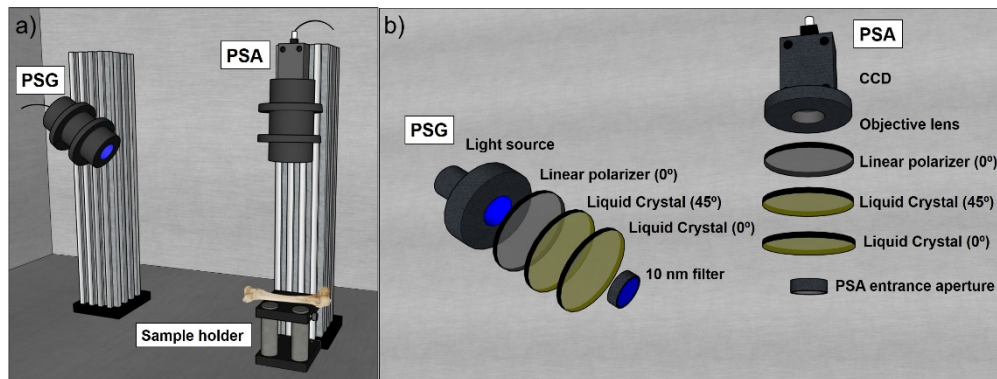


Fig. S1. a) 3D representation of the complete image Mueller polarimeter used in this study, b) 3D representation of the arrangement of the optical components in the PSG and the PSA.

In the employed set-up, the illumination is performed by using a four-wavelength high-power Thorlabs LED source (LED4D211, operated by DC4104 drivers distributed by Thorlabs), complemented with 10 nm dielectric bandwidth filters for green (530 nm) and blue (470 nm) wavelengths (Thorlabs FB530-10 and FB470-10, respectively). In counterpart, imaging is performed by means of a TECHSPEC® high-resolution objective (distributed by Edmund Optics) with a 35 mm focal length so a resolution of $22\ \mu\text{m}$ is achieved followed by an Allied Vision Manta G-504B CCD camera.

To build the experimental Mueller matrix, at least 16 independent measurements are required (related with different Stokes generation, PSG, and detection, PSA, configurations). In the current study, we use 6 illumination states of polarization (generators) and 6 detection analyzers instead, so taking 36 images, to minimize the measurement noise of each sample's Mueller matrix. A complete Mueller measurement waiting time lasts ~ 3.6 seconds: liquid crystal molecules rearrange the orientation process from one polarization state to the following one lasts approx. 100 ms.

2. Histological process of samples

For histological countercheck of the images, samples were obtained from regions analogous to the ones submitted to polarimetric analysis (i.e., striated muscle, tendon, myotendinous junction and diaphyseal bone). After extraction, they were immersion-fixed in 4% formaldehyde overnight and dehydrated through a protocol including immersion in: 70% Ethanol (30'), 80% Ethanol (30'), 90% ethanol (30'), 95% ethanol (30'), two successive immersions in 100% Ethanol (60' each) and xylene (60' each). After dehydration, they were embedded and in a paraffin wax. After cooling they were sliced in 5µm-thick sections through microtomy. Sections were mounted in crystal slides which were stained after deparaffination. Deparaffination protocol includes a 24-hour immersion in xylene and brief, successive rinses in 96% ethanol, 90% ethanol, 80% ethanol, 70% ethanol and distilled water. Two different histological staining-techniques were used.

a) Hematoxylin-eosin is the standard histological technique for diagnostic microscopy. It involves the combined use of an oxidized cationic colorant (hematoxylin) that highlights nucleic acid-rich regions of the tissue in purple and an anionic colorant (eosin) that stains in a characteristic pink color protein-rich area of the tissue, e.g. collagen in pale pink and muscle in dark pink. Sections were immersed in a bath containing Harris hematoxylin solution for 10' (Merck ® H9627), differentiated in 1% acid alcohol solution (5 ml of 37% HCl in 495 ml of 70% ethanol) for around 20", blued in a bluing solution for 20" (Sigma-Aldrich ® S5134) and counterstained with Eosin Y for 1' (Sigma-Aldrich ® E4009). Brief rinses in tap water were performed between each step.

b) Masson technique allows the differential staining of connective tissue. It includes Weigert's hematoxylin (a variant of hematoxylin) for nuclei acid-rich regions, acid fuchsin as an acid dye for protein-rich cytoplasm, a combination of phosphotungstic and phosphomolybdic acids to remove the excess fuchsin from fibers and aniline blue to counterstain the fibers. Overall, it provides a blueish color to collagen-rich tissue and deep red color to muscle fibers, also allowing the identification of other kinds of tissue. Staining protocol includes a 5' rinse in Weigert Hematoxylin (Merck® 115973), a 5' incubation in acid fuchsin solution (Sigma-Aldrich ® F8219), successive incubations (no longer than 3') in a 20% solution of phosphotungstic-phosphomolybdic acid in ethanol (Sigma-Aldrich ® 319279) and a 5' incubation in a 2.5% solution of aniline blue prepared in 2% acetic acid (Sigma-Aldrich ® B8563). If necessary, a rapid rinse in 1% acetic was performed to remove the excess dye. Brief rinses in distilled water were performed between steps.

After staining, samples were dehydrated in ethanol (5' in ascending concentrations of 70%, 80%, 90%, 96%, 100%) and xylene before being covered using Eukitt® as mounting media. After drying for 24 hours, sections were scanned (Zeiss AxioScan ®) and analyzed using a QuPath free software. Obtained images are presented in Figs. S2 and S3.

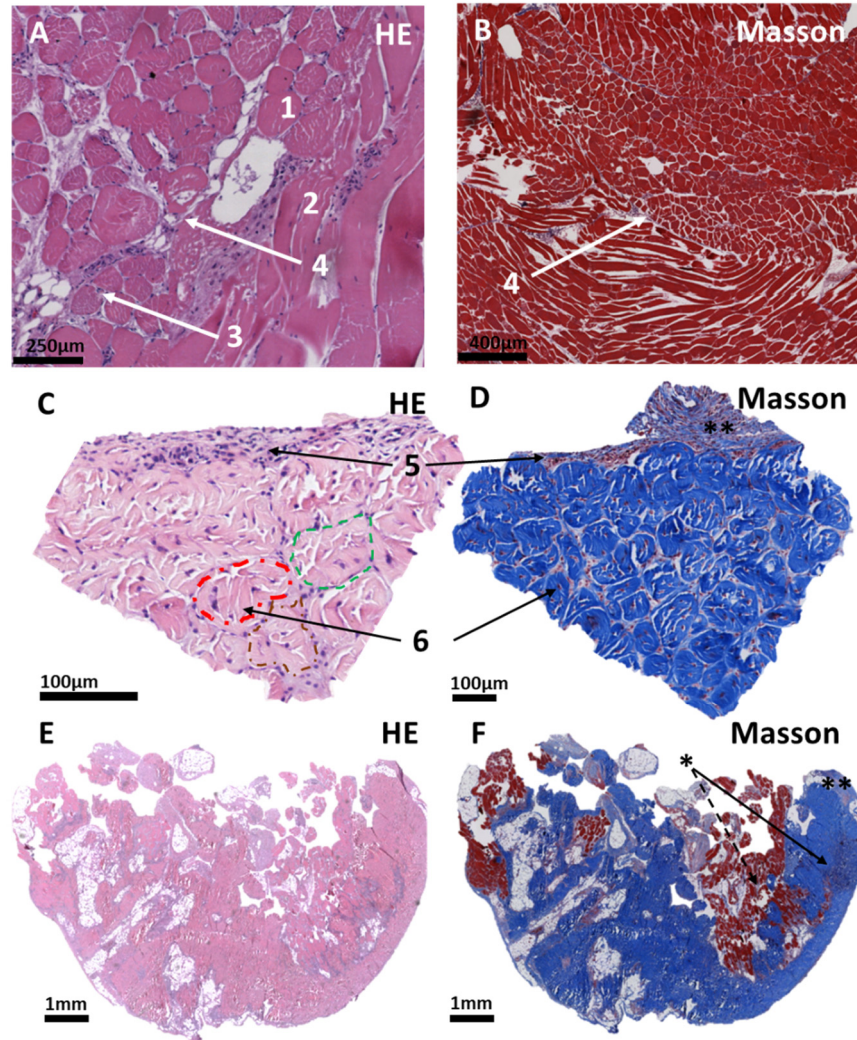


Fig. S2: Histochemical stainings of muscle (A, B), tendon (C, D) and myotendinous junction (E, F). Bundles (1, 2, 6) of either contractile (A, B, E, F) or dense fibrous (collagen) tissue (C-F) are surrounded by sheets of lax connective tissue (collagen) concentrically organized as epimysium (**)/epitenon (**), perimysium/peritenon (5) and endomysium/endotenon (6). In E, F a transverse section of the myotendinous junction is shown, where the Masson staining reveals the intermixed (*) fascicles of contractile fibers (discontinuous arrow in (F) and collagenous fibers (arrow in F)). Different fascicles of tendinous collagen are highlighted in red, green and gold (C).

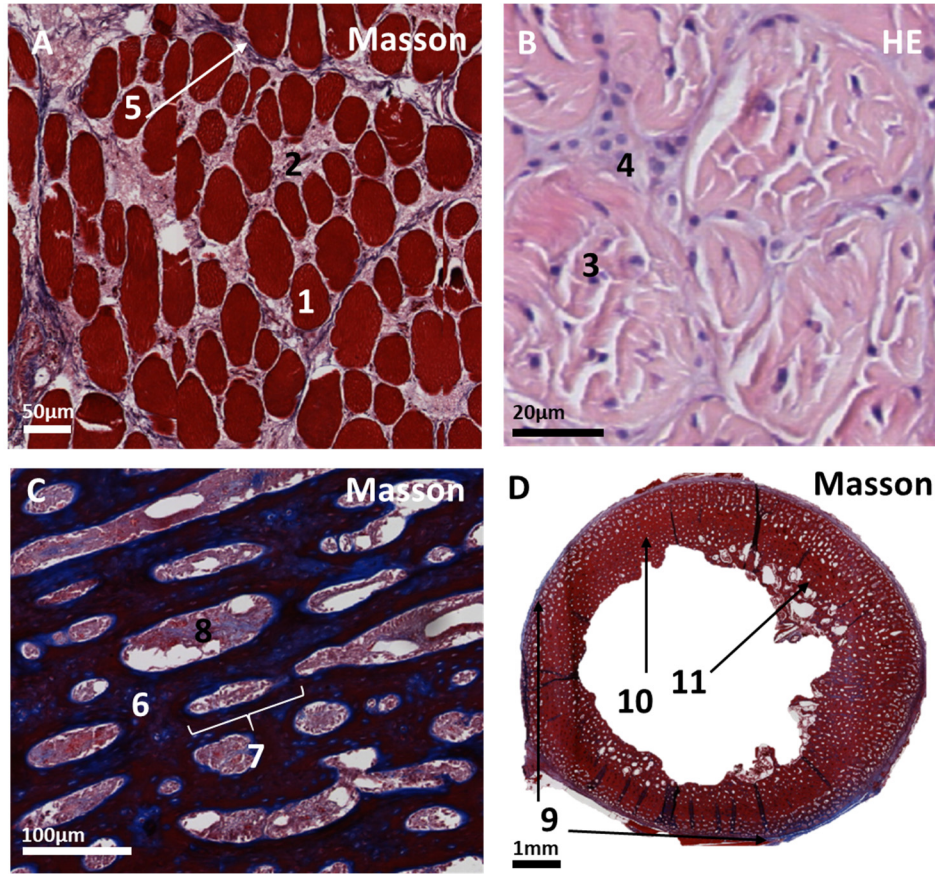


Fig. S3: Transversal section of striated muscle (A) showing bundles of contractile fibers (red colored, 1) surrounded by endomysium (2, compare to 3, 4) and included in a single fascicle surrounded by collagen (perimysium, 5). This structure is analogous to the tendinous structure (B), where the collagen fibers (3) are densely packed into a sheet of peritenon (4). Longitudinal section of cortical bone (C), showing bony matrix (6) and lacunae (7) containing osteocytes, vessels and collagen that are heavily artifacted due to pre-treatment (8); Transverse section through the diaphysis of a long bone (D), where collagenic periosteum (9), cortical bone (10) and rests of trabecular bone (11) are arranged in a concentric layers. Note the regular arrangement of lacunae, both in longitudinal and transverse sections. Color (from reddish to purple) depends on the amount of mineral deposits in any given region of the bone.

3. Experimental Mueller matrices

The experimental typical Mueller matrices (MMs) obtained for each type of tissue (muscle, tendon, myotendinous junction and bone) measured at 625 nm illumination wavelength are shown below followed by the respective parameters (P_A , P_I , P_2 , P_3 , P , R , D , δ and Ψ) resulting from matrix decomposition. The obtained images correspond to a region of interest (ROI) of 512 x 512 pixels which corresponds to an area of 1.1 x 1.1 cm².

Particularly, typical MM of muscle tissue and the respective polarimetric parameters are shown in Figs. S4 and S5, respectively. MMs of tendon, myotendinous junction and bone tissue are presented in Figs. S6 and S7, Figs. S8 and S9, and Figs. S10 and S11, respectively.

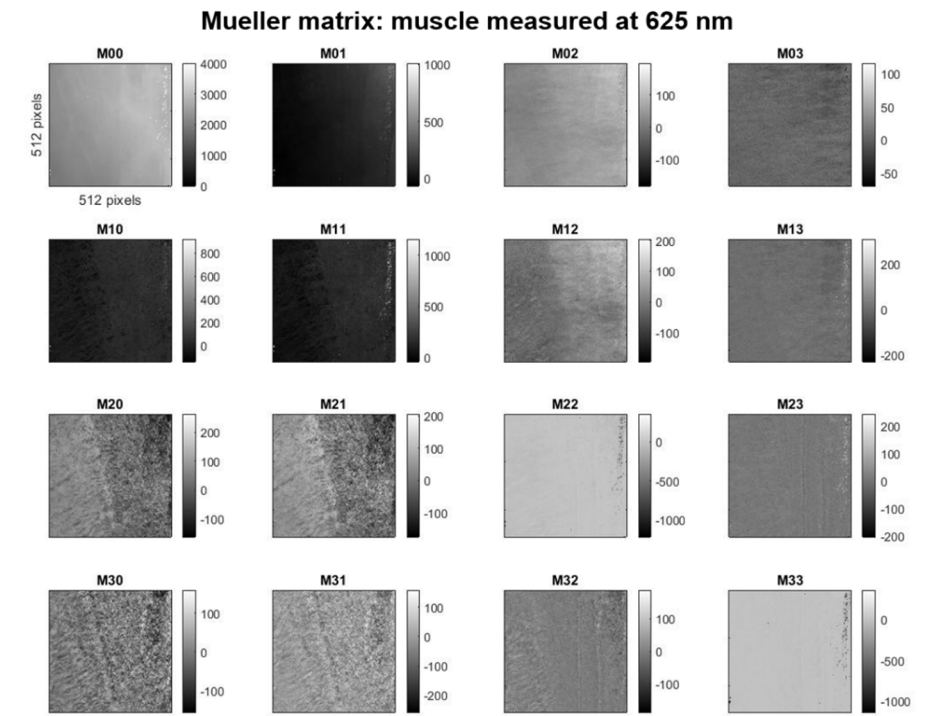


Fig. S4. Experimental Mueller matrix image of a sample of muscle tissue.

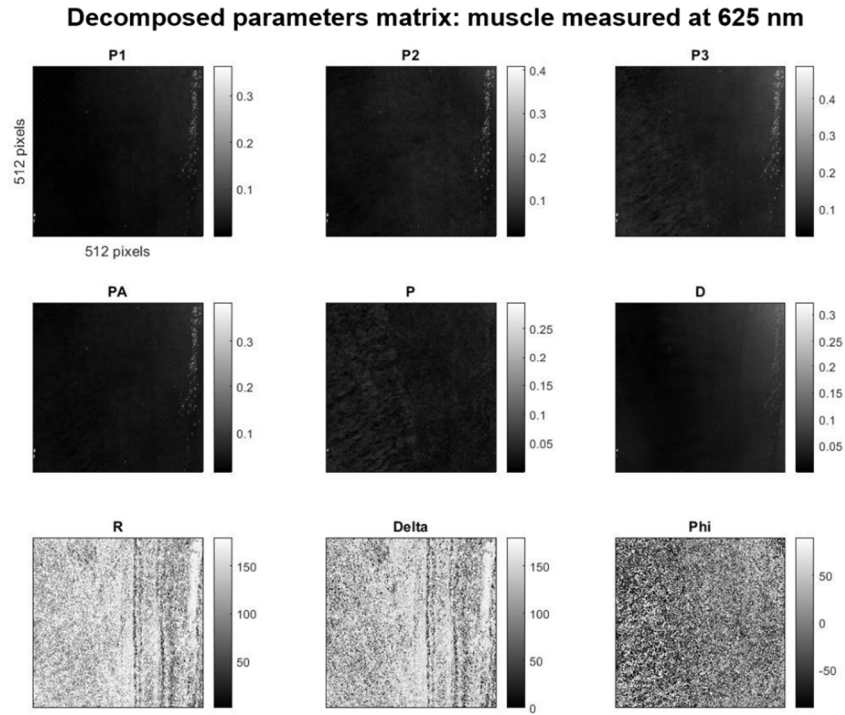


Fig. S5. Images of the polarimetric parameters P_A , P_1 , P_2 , P_3 , P , R , D , δ and Ψ from a sample of muscle tissue.

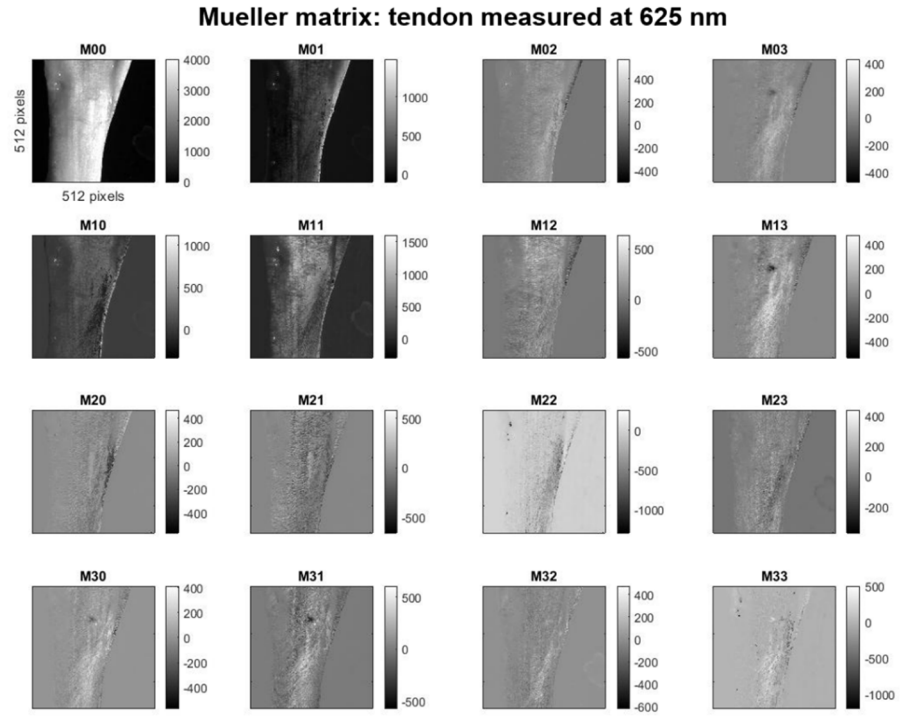


Fig. S6. Experimental Mueller matrix image of a sample of tendon tissue.

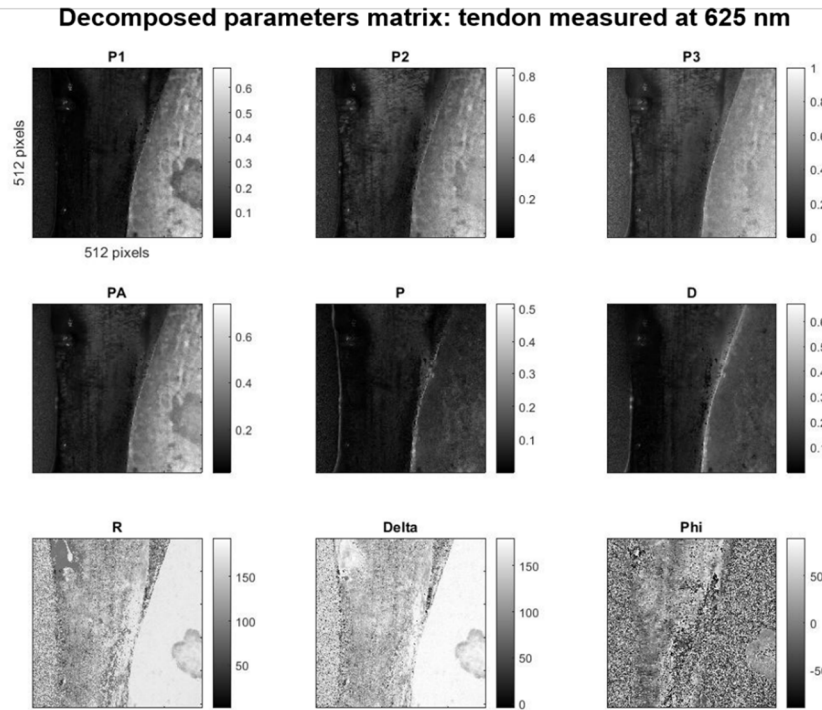


Fig. S7. Images of the polarimetric parameters P_A , P_I , P_2 , P_3 , P , R , D , δ and Ψ from a sample of tendon tissue.

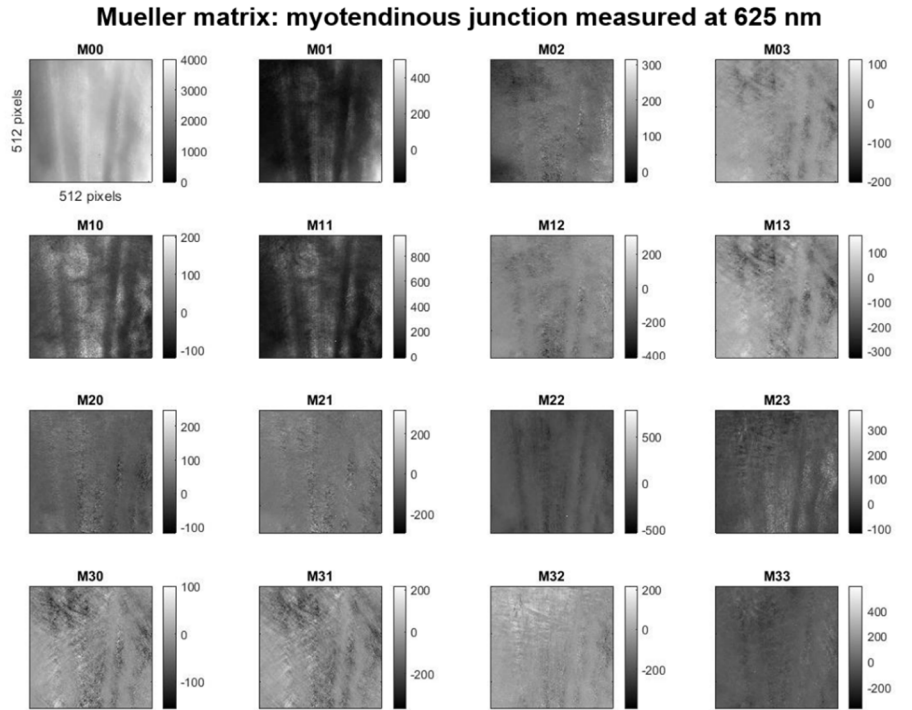


Fig. S8. Experimental Mueller matrix image of a sample of myotendinous tissue.

Decomposed parameters matrix: myotendinous junction measured at 625 nm

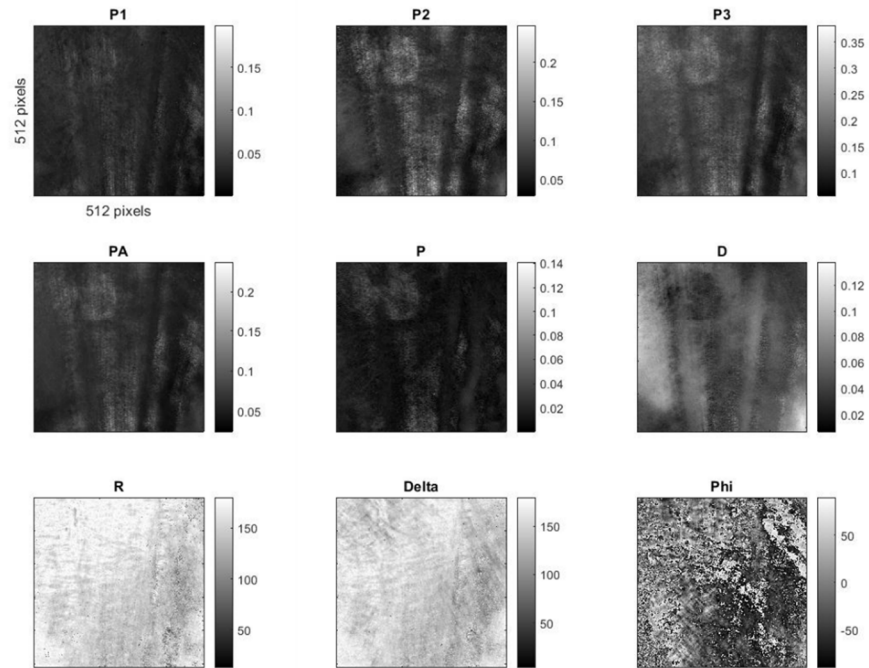


Fig. S9. Images of the polarimetric parameters P_A , P_t , P_2 , P_3 , P , R , D , δ and Ψ from a sample of myotendinous tissue.

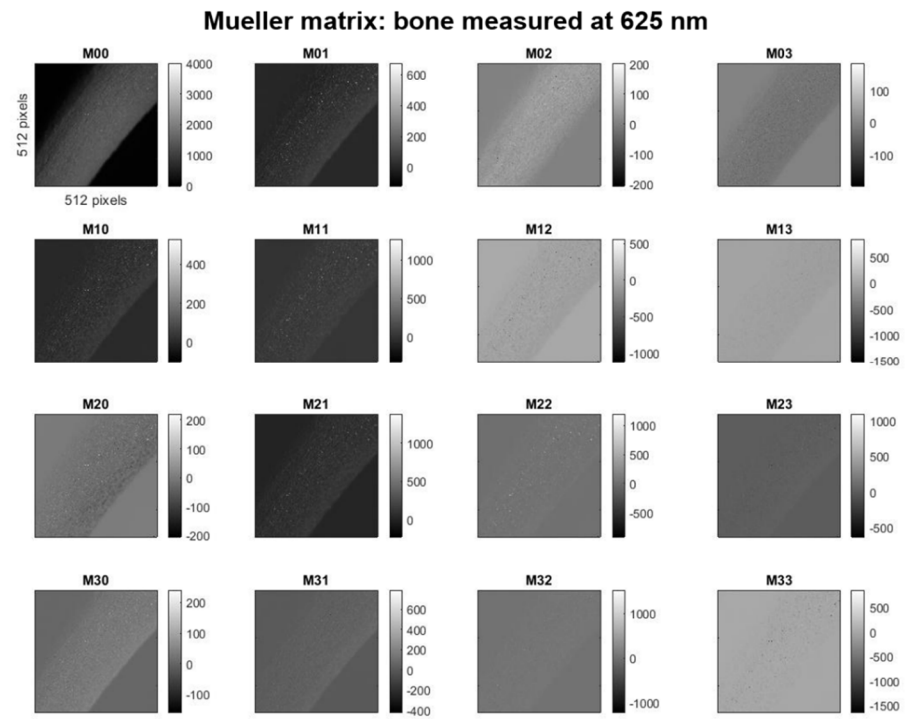


Fig. S10. Experimental Mueller matrix image of a sample of bone tissue.

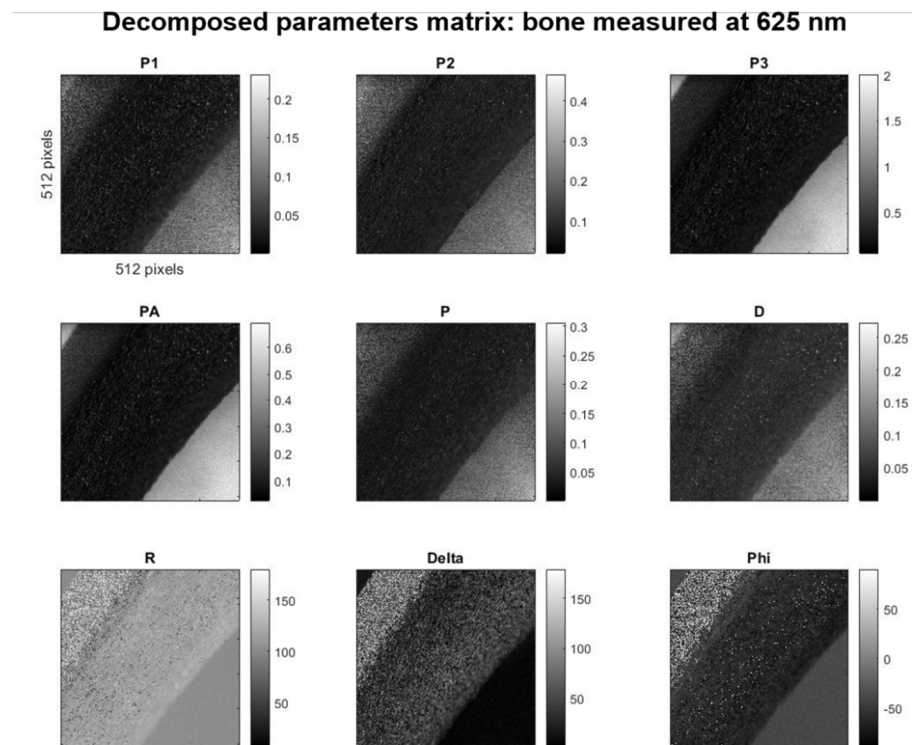


Fig. S11. Images of the polarimetric parameters P_d , P_l , P_2 , P_3 , P , R , D , δ and Ψ from a sample of bone tissue.

4. Statistical analysis

For the correct manipulation of data to construct a predictive model it is mandatory to know which are the distributions profile (parametric or not) and, depending on the results, apply the corresponding statistical tests to formulate the tissue-discrimination functions. In this way, we perform an exploratory univariant analysis (to analyze the distribution profile) and a posterior factor analysis with principal components extraction for the dichotomic predictive models' construction. The additional material for the above-mentioned analysis is described in the following sections.

4.1 Exploratory univariant analysis

To ensure the correct statistical manipulation of polarimetric data distributions classified by type-of-tissue variable groups, it is necessary to previously perform an exploratory univariant analysis based on the study of the graphical differences between sample's distributions, as well as the central tendency, data dispersion, asymmetry and outlier's identification by means of Boxplot [5,6].

Recalling the P_2 purity index (measured at 625 nm illumination) presented in Fig. 2, in this section we provide, in complement, the results in the format of Boxplots corresponding to the data acquired at 530 nm and 470 nm in Figs. S12 and S13, respectively.

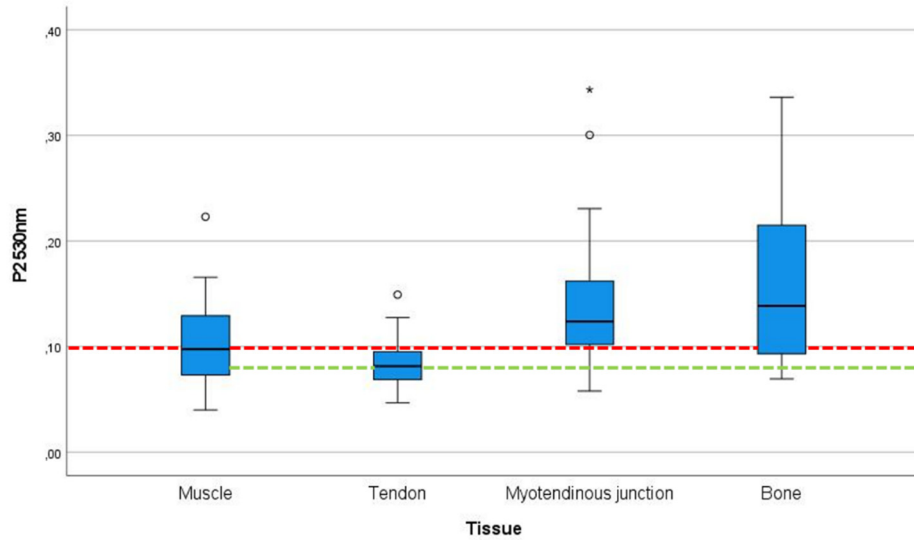


Fig. S12. Boxplot of P_2 index for all tissues measured at 470 nm illumination channel. Red-dashed line visually represents the potential of the metric to discriminate muscle among remaining tissue types: the median of the muscle box does not fit within the other tissues' boxes. Green-dashed line visually represents P_2 tendon discrimination capability. Boxplot points out the low quantity of outliers on data distributions (which can be extrapolated to the remaining metrics): mild and extreme values are represented by circles and stars, respectively.

The exposed P_2 data distributions for all type of tissues measured at 530 nm wavelength (Fig. S12) clearly shows the same small number of outliers' behavior as 625 nm (manuscript Fig. 2) and 470 nm (Fig. S13). What is more, asymmetric tendency (position of the median is not in the middle of boxes) is common for all wavelengths. Moreover, tissue discrimination capability of P_2 is pointed out (median line does not fit within the remaining boxes): at 530 nm illumination (Fig. S12), the metric shows muscle discriminative potential (see dashed red line) but also tendon differentiation from myotendinous junction and bone (see dashed green line). At 470 nm

illumination conditions (Fig. S13), P_2 keeps differentiating muscle (see dashed red line) but also works well as a myotendinous junction discriminator (see dashed blue line).

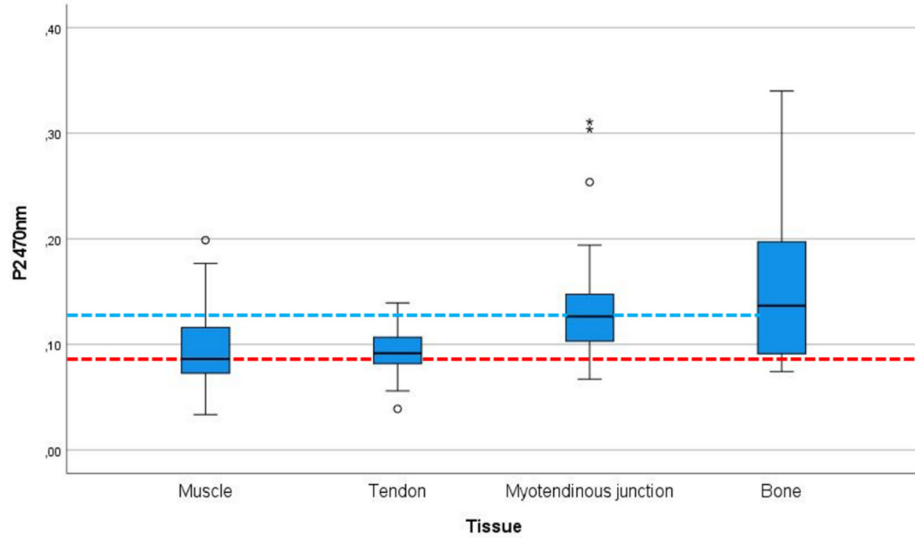


Fig. S13. Boxplot of P_2 index for all tissues measured at 470 nm illumination channel. Red-dashed line visually represents the potential of the metric to discriminate muscle among remaining tissue types: the median of the muscle box does not fit within the other tissues' boxes. Blue-dashed line visually represents P_2 Myotendinous junction discrimination capability. Boxplot points out the low quantity of outliers on data distributions (which can be extrapolated to the remaining metrics): mild and extreme values are represented by circles and stars, respectively.

For the Kruskal-Wallis [7,8] homogeneity multiple contrast analysis, the output significance of the 27 measured polarimetric indicators for each pair of tissue discriminative power is presented in Table S1. Particularly, we assume, as null hypothesis, that the data comes from samples with the same statistical distribution. By setting a significance level, α , of 0.05, Kruskal-Wallis outcomes reject, in most of the cases, the mentioned hypothesis: p-values lower than the significance level show the discriminatory potential of the polarimetric indicator between the corresponding pair of tissues. Note that, because the SPSS software found no significant difference when sorting by pair of tissues, only one value is output for optical rotation, Ψ .

Table S1. Significance (p-value, rounded to three digits) of the M-metrics pair-of-tissue discrimination.

		<i>Muscle – Tendon</i>	<i>Muscle – Myo.</i>	<i>Muscle – Bone</i>	<i>Tendon – Myo.</i>	<i>Tendon – Bone</i>	<i>Myo. – Bone</i>
625 nm	P_d	0.000	0.000	0.000	0.559	0.331	0.599
	P_l	0.000	0.000	0.000	0.210	0.274	0.948
	P_2	0.003	0.000	0.000	0.741	0.181	0.254
	P_3	0.000	0.000	0.000	0.723	0.714	0.936
	P	0.427	0.000	0.000	0.036	0.000	0.004
	R	0.378	0.000	0.000	0.002	0.000	0.223

	D	0.070	0.002	0.000	0.149	0.008	0.135
	δ	0.374	0.005	0.000	0.062	0.004	0.614
	Ψ	0.110					
530 nm	P_A	0.351	0.000	0.000	0.000	0.000	0.730
	P_I	0.594	0.000	0.000	0.000	0.000	0.389
	P_2	0.044	0.000	0.000	0.000	0.003	0.982
	P_3	0.995	0.000	0.000	0.000	0.000	0.268
	P	0.054	0.001	0.000	0.062	0.001	0.436
	R	0.001	0.000	0.000	0.358	0.210	0.615
	D	0.695	0.017	0.010	0.060	0.031	0.534
	δ	0.008	0.000	0.000	0.283	0.042	0.247
	Ψ	0.101					
470 nm	P_A	0.480	0.000	0.000	0.000	0.000	0.877
	P_I	0.253	0.000	0.000	0.000	0.000	0.436
	P_2	0.930	0.000	0.000	0.000	0.000	0.885
	P_3	0.340	0.000	0.000	0.000	0.000	0.508
	P	0.010	0.020	0.000	0.835	0.001	0.015
	R	0.024	0.002	0.002	0.358	0.211	0.616
	D	0.383	0.021	0.000	0.181	0.005	0.079
	δ	0.009	0.004	0.009	0.749	0.634	0.830
	Ψ	0.299					

4.2 Principal Components extraction and component score coefficient matrix

Linked with scree plot [9], Table S2 exposes the eigenvalues of the chosen 10 principal components [10,11], together with the data variance and the cumulative variance (both in %). Note that C_1 carries the highest amount of explained variance. This behavior will be reflected in predictive model construction as this component is going to have a strong influence. Lower amounts of variance are taken by the remaining components. However, it is important to remark that when considering the 10 components as a whole, we achieve a 92% of explained variance.

Table S2. Percentage of variance explained.

	Extraction Sums of Squared Loadings		
	<i>Total</i>	<i>% of Variance</i>	<i>Cumulative</i>
C_1	11.195	41.462	41.462
C_2	3.783	14.012	55.473
C_3	2.265	8.391	63.864
C_4	2.008	7.436	71.300

C_5	1.786	6.616	77.915
C_6	1.026	3.799	81.714
C_7	0.890	3.298	85.012
C_8	0.762	2.824	87.836
C_9	0.634	2.350	90.186
C_{10}	0.509	1.885	92.071

The 27-dimension metrics space is reduced to a new 10-dimension principal components space. In this way, the original polarimetric information is encoded on the principal components: we can write each component as a linear combination of the 27 different polarimetric indicators weighed by some constants provided by columns of the so-called component score coefficient matrix, shown in Table S3.

Table S3. Component score coefficient matrix of the 10 first principal components.

		Principal component									
		C_1	C_2	C_3	C_4	C_5	C_6	C_7	C_8	C_9	C_{10}
625 nm	P_A	0.068	-0.083	0.219	-0.061	0.113	0.005	-0.079	-0.050	-0.066	-0.204
	P_1	0.066	-0.020	0.154	-0.126	0.205	-0.024	-0.128	0.090	-0.129	-0.178
	P_2	0.063	-0.103	0.214	-0.017	0.053	0.013	-0.015	-0.162	-0.035	-0.241
	P_3	0.063	-0.090	0.230	-0.060	0.102	0.022	-0.088	-0.026	-0.053	-0.146
	P	0.013	-0.092	0.097	-0.205	0.168	0.441	0.442	0.329	0.252	0.217
	R	0.036	0.154	0.138	-0.032	0.117	-0.329	-0.074	-0.018	0.484	0.636
	D	0.028	-0.107	0.218	0.232	-0.213	-0.082	0.032	-0.252	0.099	-0.077
	δ	0.034	0.160	0.139	-0.098	0.018	-0.114	-0.014	0.402	-0.505	0.532
	Ψ	-0.011	0.037	0.008	0.280	0.196	-0.313	0.434	0.472	0.120	-0.622
530 nm	P_A	0.085	-0.003	-0.105	0.008	0.017	-0.096	-0.044	-0.076	-0.058	0.018
	P_1	0.082	0.027	-0.069	0.005	0.045	-0.127	0.020	-0.029	-0.011	-0.044
	P_2	0.082	-0.021	-0.095	0.019	-0.023	-0.077	-0.072	-0.121	0.066	-0.002
	P_3	0.078	-0.009	-0.132	-0.010	0.035	-0.085	-0.062	-0.094	-0.201	0.083
	P	0.068	0.008	-0.094	-0.016	0.066	-0.004	0.434	-0.315	-0.235	0.111
	R	0.038	0.180	0.105	0.037	-0.038	-0.154	0.250	-0.400	0.294	-0.022

470 nm	D	0.043	-0.118	0.089	0.196	-0.245	0.034	0.036	0.239	0.073	0.484
	δ	0.029	0.179	0.111	0.038	-0.156	0.038	0.294	-0.065	-0.553	-0.164
	Ψ	-0.001	0.060	-0.005	0.346	0.298	0.145	-0.064	0.098	0.008	0.251
	P_A	0.083	0.008	-0.127	0.005	-0.011	0.027	-0.121	0.169	0.079	-0.117
	P_1	0.080	0.035	-0.101	0.005	0.005	0.007	-0.143	0.287	0.111	-0.099
	P_2	0.081	-0.010	-0.136	0.007	-0.033	0.051	-0.106	0.082	0.097	-0.152
	P_3	0.080	0.000	-0.126	-0.002	-0.003	0.017	-0.113	0.124	0.030	-0.065
	P	0.057	-0.027	-0.143	-0.026	0.000	0.244	0.459	-0.190	0.108	0.216
	R	0.033	0.181	0.084	-0.034	-0.119	0.283	-0.083	0.023	0.616	-0.241
	D	0.049	-0.122	0.036	0.184	-0.239	0.002	0.095	0.258	0.005	0.254
	δ	0.025	0.179	0.062	0.012	-0.233	0.356	-0.087	0.196	-0.149	-0.308
	Ψ	0.006	0.054	0.017	0.303	0.236	0.444	-0.235	-0.285	-0.176	0.151

5. Predictive model construction

To test the goodness-of-fit of the four constructed predictive models (muscle, tendon, myotendinous junction and bone), we rely on the Hosmer-Lemeshow [12] significance and the R^2 of Nagelkerke [13] measure. Outputs are presented in Table S4.

Table S4. Hosmer-Lemeshow significance (p-value) and R^2 of Nagelkerke, of each predictive model.

	Muscle	Tendon	Myotendinous junction	Bone
<i>Hosmer-Lemeshow Sig.</i>	0.192	0.980	0.530	0.956
<i>R^2 of Nagelkerke</i>	0.640	0.690	0.282	0.481

Because the obtained Hosmer-Lemeshow [12] significance values are larger than the threshold (p-value > 0.05), we accept the null hypothesis: all the four predictive models fit the data. Regarding to the of R^2 of Nagelkerke [13] values, the larger the value the better the fit, being 1 the maxim value (optimal fit). However, generally speaking, R^2 of Nagelkerke values larger than 0.2 are acceptable, and larger than 0.6 can be associated to excellent fits. In this vein, obtained results show a nice data fit for the muscle (0.64), tendon (0.69) and bone (0.48) regressions. In turn, the myotendinous junction data regression lead to an acceptable result (0.28), but clearly worst than those obtained for the other tissues. This result is in agreement with the models analysis provided in the main manuscript, where the worst results in terms of sensitivity and specificity are obtained for the myotendinous junction model.

6. Tissue recognition through binary logistic model

For a complementary visual analysis, the output of the probabilistic model for the particular cases of an arbitrary bone and an arbitrary myotendinous junction tissue are provided in Figs.

S14 and S15, respectively. Particularly, Fig. S14 shows the intensity image M00 (Fig. S14(a)) and the four probability function images (muscle, tendon, myotendinous junction and bone recognition (Figs. S14(b-e), respectively) for a bone sample. Recall that sample holder polarimetric information is not characterized: pixel values for background acquired data have no physical meaning. The obtained probability function images show how the bone model successfully recognize the bone tissue pixels (Fig. S14(e)), clearly showing, in addition, the two longitudinal bone edges (marked with yellow and red dotted lines) not visible in intensity image in Fig. S14(a). When analyzing the probability distribution of the three remaining functions, a good discriminating potential is demonstrated, specially for the tendon model in Fig. S14(c), which clearly does not recognize the tissue as tendon. On the other hand, muscle and myotendinous junction probability images (Figs. S14(b) and S14(d)) show, with low probability values, an overall discard of analyzed tissue to be muscle or myotendinous junction tissues, respectively. As in previous discussion, worst predictive results are obtained for the myotendinous junction model (Fig. S14(d)).

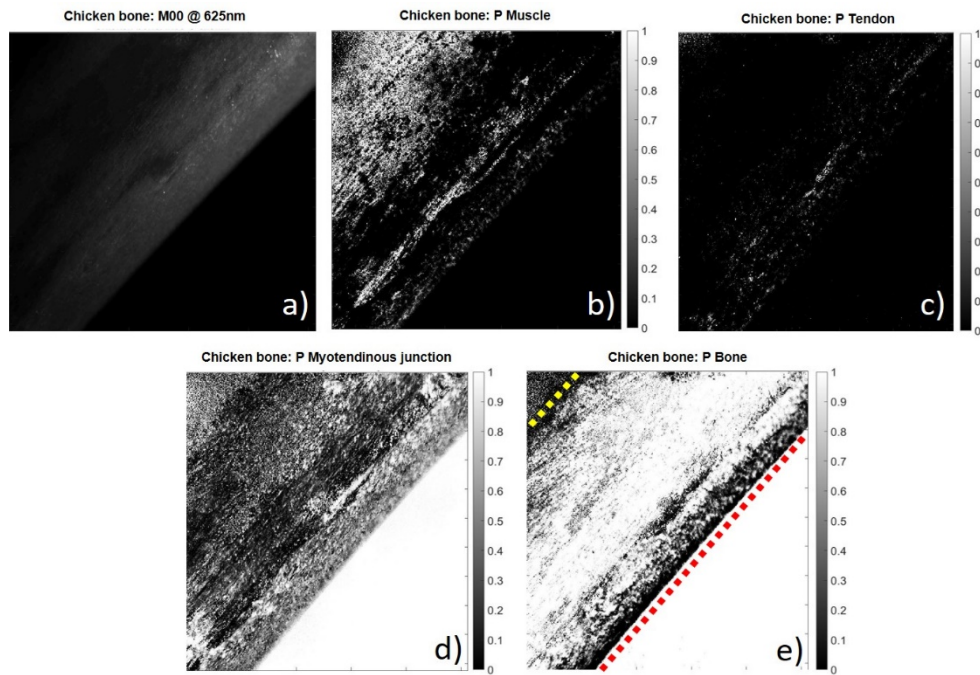


Fig. S14. Intensity image M00 (a) and probability function of muscle (b), tendon (c), myotendinous junction (d) and bone (e) for chicken bone measurements. The gray level bars, placed to the right of the corresponding probability function images, defines whether the probability of the pixel to be recognized as a particular tissue is one (white) or zero (black). Yellow and red dotted lines highlight the position of the edges of the bone.

Analogously, Fig. S15 shows the intensity image M_{00} (Fig. S15(a)) and the four probability function images (muscle, tendon, myotendinous junction and bone recognition (Figs. S15(b-e), respectively) for a particular myotendinous junction sample. The obtained probability images when measuring the myotendinous junction sample demonstrate how all the models discard the analyzed myotendinous junction tissue to be muscle (Fig. S15(b)), tendon (Fig. S15(c)) or bone (Fig. S15(e)), except the actual myotendinous junction model (Fig. S15(d)), who successfully identify the tissue as myotendinous junction one. Therefore, the overall recognition of the tissue is correct, as the above-stated results are consistent in most image pixels. Only few individual pixels throughout the images show deviation from the general tendency, but still they could be properly categorized depending on the selected categorization probability threshold selected.

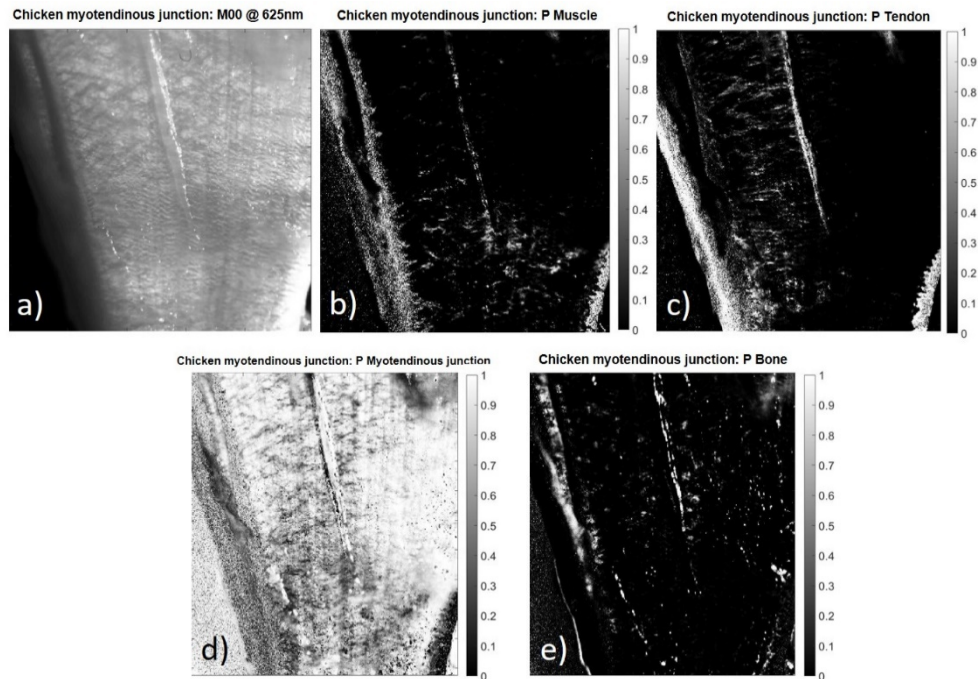


Figure S15. Intensity image M00 (a) and probability function of muscle (b), tendon (c), myotendinous junction (d) and bone (e) for chicken myotendinous junction measurements. The gray level bars, placed to the right of the corresponding probability function images, defines whether the probability of the pixel to be recognized as a particular tissue is one (white) or zero (black).

7. References

1. A. Van Eeckhout, A. Lizana, E. Garcia-Caurel, J.J. Gil, A. Sansa, C. Rodríguez, I. Estévez, E. González, J.C. Escalera, I. Moreno, and J. Campos, "Polarimetric imaging of biological tissues based on the indices of polarimetric purity," *Journal of Biophotonics*, e201700189 (2017).
2. A. Van Eeckhout, A. Lizana, E. Garcia-Caurel, J.J. Gil, R. Ossikovski, and J. Campos, "Synthesis and characterization of depolarizing samples based on the indices of polarimetric purity," *Opt. Lett.* **42**(20), 4155-4158 (2017).
3. A. Van Eeckhout, E. Garcia-Caurel, R. Ossikovski, A. Lizana, C. Rodríguez, E. González-Arnav, and J. Campos, "Depolarization metric spaces for biological tissues classification," *Journal of Biophotonics*, e202000083 (2020).
4. A. Van Eeckhout, E. Garcia-Caurel, T. Garnatje, M. Dufort, J. C. Escalera, J. Vidal, J. J. Gil, J. Campos, and A. Lizana, "Depolarizing metrics for plant samples imaging," *PLoS ONE* **14**(3), e0213909 (2019).
5. J. E. V. Ferreira, M. T. S. Pinheiro, W. R. S. D. Santos, and R. D. S. Maia, "Graphical representation of chemical periodicity of main elements through Boxplot," *Educación Química* **27**(3), 209-216 (2016).
6. R. McGill, J. W. Tuckey, and W. A. Larsen, "Variations of Box Plots," *The American Statistician* **32**(1), 12-16 (1978).
7. S. Guo, S. Zhong, and A. Zhang, "Privacy-preserving Kruskal-Wallis test," *Computer Methods and Programs in Biomedicine* **112**(1), 135-145 (2013).
8. G. D. Ruxton, and G. Beauchamp, "Some suggestions about appropriate use of the Kruskal-Wallis test," *Animal Behaviour* **76**(3), 1083-1087 (2008).
9. M. Zhu, and A. Ghodsi, "Automatic dimensionality selection from the Scree plot via the use of profile likelihood," *Computational Statistics and Data Analysis* **51**(2), 918-930 (2006).
10. H. H. Jolliffe, "Principal Component Factor Analysis," *All Graduate Plan B and other Reports*, 1117 (1968).

11. C. C. Clark, C. M. Barnes, M. J. Duncan, H. D. Summers, and G. Stratton, "Physical activity, motor competence and movement and gait quality: A Principal Component Analysis," *Human Movement Science* **68**, 102523 (2019).
12. Y. Tahtali, "Use of Factor Scores in Multiple Regression analysis for estimation of body weight by certain body measurements in Romanov Lambs," *PeerJ*, **7**, e7434 (2019).
13. N. J. D. Nagelkerke, "A note on the general definition of the coefficient of determination," *Biometrika*, **78**(3), 691–692 (1991).